Chapter-5

NUCLEUS-ACOUSTIC WAVES IN DEGENERATE ONe AND CO WHITE DWARF CORES AND NEARLY DEGENERATE ENVELOPES

Abstract: *This Chapter presents a theoretic investigation to analyze the low-frequency nucleus-acoustic waves excitable in the completely degenerate cores of ONe (oxygen-neon) and CO (carbon-oxygen) white dwarfs and their nearly degenerate envelopes*[†]*. We use a quantum hydrodynamic formalism to model the complex system dynamics comprising of the electronic species, light nuclear species, and heavy nuclear species. The inner concentric layer-wise electronic pressures are judiciously modelled. The electronic energy distribution, governed by the Fermi-Dirac thermostatistical distribution law, involves both the thermodynamical temperature and chemical potential. It emphasizes on the transition state between the thermodynamical temperature (classical) and the Fermi temperature (quantum) for the borderline regions of intermediate degeneracy for the first time. The model closure is obtained with the help of the gravito-electrostatic Poisson formalism. A normal Fourier-centric spherical mode analysis procedurally yields a generalized linear dispersion relation (sextic in degree). A numerical illustrative platform is employed to highlight the nucleus-acoustic wave propagatory and dispersive features. It is demonstrated that the nucleus-acoustic wave in ONe (CO) white dwarfs exhibits sensible growth features in the transcritical (supercritical) wave space. Its temperature-sensitivity is more (less) prominent in ONe (CO) white dwarfs, and so forth. In distinction, a full nucleus-acoustic wave dispersion portrayal is illustratively presented and interpreted. The astronomical circumstances sensible to the presented explorative study are finally outlined.*

5.1 INTRODUCTION

This is a well-known fact that white dwarfs are the end products of stellar evolution for most of the low and medium mass main-sequence stars [1, 2]. After the thermonuclear hydrogen fusion ceases, the temperature of the stellar core is sufficient to fuse helium

[†] Dasgupta, S., Atteya, A., and Karmakar, P. K. Modal stability of low-frequency nucleus-acoustic waves in completely degenerate dwarf cores and their nearly degenerate surroundings. *Chinese Journal of Physics* 83: 539-557, 2023.

(He), resulting in the formation of carbon (C) and oxygen (O). The outer layers expand and cool, thereby leading to the formation of a red giant. The star then sheds its outer layers, forming a gaseous shell (planetary nebula) around the core [3]. This remnant core, with no nuclear fuel left for burning to counter the inward self-gravity action, forms white dwarf. As the core is usually made up of C and O, it forms CO white dwarf [3-5]. For massive stars having masses (M) in the range $8M_{\odot} \lesssim M \lesssim 11M_{\odot}$ (where, $M_{\odot} = 1.98 \times 10^{30}$ kg is the solar mass), the temperature is sufficient to fuse C, but not neon (Ne), leading to the formation of ONeMg cores of white dwarfs [6, 7].

As stated in the previous chapters, white dwarfs are supported against gravity by means of their electron degeneracy pressure. The electron degeneracy pressure is a purely quantum pressure with no classical analog. In addition to the electron degeneracy pressure, there are several other important quantum effects that must be taken into account to get a view of the all the quantum-mechanical effects acting on the system. Some such effects are the exchange and correlation effects. The exchange energy is a direct consequence of the Pauli exclusion principle [8, 9]. As a result, electrons with same spin tend to repel each other. As such, it reduces the Coulomb repulsion that would otherwise exist between them in absence of the same spin condition [8, 9]. Correlation interaction gives a metric to determine how much the mobility of one electron is influenced by the presence of the surrounding electrons [9-11]. Mathematically, correlation energy is the difference between the total electronic energy and the energy obtained from Hartree-Fock approximation after simplifying a many-body quantum-mechanical system into an equivalent single one via the Slater determinant [11]. A large number of investigations in a wide variety of domains, ranging from nanoscales-to-waves and instabilities in compact astrophysical objects [12-25] have been reported taking into account the exchange and correlation effects.

In our proposed semi-analytic study, we investigate the excitation, propagation, and dispersion characteristics of the nucleus-acoustic waves. It is pertinent to add that the nucleus-acoustic wave of current concern is of a hybrid hydrokinetic type. The considered system refers to the completely degenerate ONe and CO cores and their nearly degenerate surrounding regions depicting the transition between thermodynamic temperature (T, classical), and Fermi temperature (T_F, quantum). It consists of three constitutive species: electrons, light nuclear species ($^{12}_{6}C$ for CO white dwarf and $^{16}_{8}O$

for ONe white dwarf), and heavy nuclear species ($^{16}_{8}O$ for CO white dwarf and $^{20}_{10}Ne$ for ONe white dwarf).

The electrons are governed by an equation of state that was developed exclusively for the study of the white dwarfs [8, 9]. The above mentioned equation of state takes into account the contribution due to the electronic pressure (degenerate Fermi pressure for the completely degenerate core and the nearly degenerate pressure for the surrounding transition region around the core), pressure due to the interaction of the electrons with other electrons and surrounding nuclei, exchange interaction, and correlation interaction, explicitly. The constitutive light nuclear species and heavy nuclear species are governed classically by an appropriate equation of state taking into account their thermal pressures.

The quantum electrons, governed by the Fermi-Dirac (FD) statistical distribution law, are characterized by two important parameters: temperature (T) and chemical potential (μ) [26-29]. In addition to the completely degenerate pressure in the core of the considered white dwarfs, our study also emphasizes on the nearly degenerate pressure in the borderline region (with an intermediate degree of degeneracy) around the core which is neither strongly degenerate, nor strongly non-degenerate. This is achieved by means of a temperature degeneracy parameter, expressed with a usual symbolism (unfolded later in the text), as $G'_e = Li_{5/2}(-\xi)/Li_{3/2}(-\xi)$ [26-29]. The degeneracy of the system is described with the help of $\xi = e^{\beta'\mu}$ (thermodynamic beta, $\beta' = 1/k_B T$), a function of μ and T [26-29]. A large number of observational evidences and stellar evolutionary models have been reported in favour of the ONeMg white dwarfs [6, 7, 30-35]. Recent model calculations have established O and Ne as the most significant components of the dwarf core, thereby reducing the Mg abundance [7], thus making it essentially an ONe white dwarf system. Likewise, several models and observational findings have also been reported in favour of the CO white dwarfs [4, 5, 34, 35]. In fact, very recently, IRAS00500+6713, an object having super-Chandrasekhar mass, has been observationally reported, which is believed to be a merger product of a ONe and CO white dwarf [35]. Thus, we see that there are quite a few numbers of studies dealing with observational and astrophysical aspects of ONe and CO white dwarfs. A large number of semi-analytic investigations on nucleus-acoustic waves have also been reported [36-39]. However, no work has been done concerning ONe and CO white

dwarfs from the plasma perspective to the best of our knowledge. This served as the main motivating force behind the conducted study. It is a well-known fact that in the process of stellar evolution, after the red giant phase, the star sheds its outer layers, forming a gaseous shell (planetary nebula) around the core [3]. This remnant core forms the white dwarf. Thus, the white dwarf is a purely quantum system due to extreme density. And the surrounding gaseous nebular shell is classically distributed due to sparse particle distribution. Thus, as we move from the classical nebular region to the quantum white dwarf region, we assume that there is no sharp demarcating boundary between the completely non-degenerate (classical) nebular region and completely degenerate (quantum) white dwarf core. Thus, there must be a transition region of intermediate degeneracy between these two domains. The main novelty of the exploration lies in the fact that it is the first study dedicated to specific white dwarf members (ONe and CO white dwarfs) from the plasma-based instability perspective. Additionally, unlike most of the previous studies available in the literature, this investigation focuses on not only the quantum core, but also the transition region of intermediate degeneracy (nearly degenerate zone) between the completely degenerate quantum core and the completely non-degenerate classical nebula for the first time to the best of our knowledge. All these points obviously strengthen the main novelty aspects of the current semi-analytic study comprehensively. Thus, the study of plasma wave excitation and propagation in these white dwarfs explicitly (completely degenerate core and nearly degenerate transition region around the core of ONe and CO white dwarfs), has still been lying as an open problem that is yet to be well-addressed. In our proposed model analysis, we investigate the same in a semi-classical and semi-analytic approach with all the said relevant realistic key factors taken into account.

5.2 PHYSICAL MODEL AND FORMALISM

We consider a theoretic quantum hydrodynamic model in a spherically symmetric geometrical construct to study the degeneracy-dependent radial white dwarf core behaviours from the nucleus-acoustic wave stability perspective. Most of the astrophysical structures, mainly the white dwarfs, are found to be spherical in shape due to the nature of gravity forces [40, 41]. Thus, the approximation of spherical symmetry (pure radial dependency) is more appropriate for modelling astrophysical bounded structures, such as white dwarfs, neutron stars, etc. The assumption of spherical

symmetry simplifies a complicated spherical three-dimensional problem into a simplified radial one-dimensional problem due to the omission of complicating polar and azimuthal counterparts. This is the basic idea behind the consideration of spherically symmetric geometry. In other words, a spherically symmetric model, with perturbations varying along the radial direction only [41], is considered in the current study due to the above reasons. The adopted model consists of three constitutive species; namely, quantum electrons, classical light nuclear species, and classical heavy nuclear species. The equation of state of the quantum electrons considers the contributions due to the electronic pressure resulting from temperature degeneracy (both completely degenerate pressure in the core and nearly degenerate pressure in the transition region around the core with the T-T_F demarcation [26], interaction of electrons with other electrons and surrounding nuclei, exchange interaction, and correlation interaction effects conjointly [8, 9]. The classical light nuclear species and heavy nuclear species are governed by a proper equation of state on their respective thermal pressures. The dynamics of all the three constitutive species are governed by the flux conservation continuity equation, force-balancing momentum equation, and their respective equations of state. The model closure is finally obtained by means of the electrostatic and self-gravitational Poisson equations dealing with the respective potential distributions originating from the corresponding density fields. The respective equations governing the electronic dynamics with all generic notations [8, 9, 36, 37] are accordingly cast as

$$\partial_t n_e + r^{-2}\partial_r\left(r^2 n_e u_e\right) = 0, \tag{5.1}$$

$$e\partial_r\phi - n_e^{-1}\partial_r P_e - \hbar^2\left(2m_e\right)^{-1}\partial_r\left(n_e^{-\frac{1}{2}}\right)\left[r^{-2}\partial_r\left\{r^2\partial_r\left(n_e^{-\frac{1}{2}}\right)\right\}\right] = 0, \tag{5.2}$$

$$P_e = P_{el} - P_{ie} - P_{exc} - P_{corr}. \tag{5.3}$$

Similarly, the basic equations governing the generalized dynamics of the classical particles (with $\alpha = l$ for light nuclear species and $\alpha = h$ for heavy nuclear species) are given as

$$\partial_t n_\alpha + r^{-2}\partial_r\left(r^2 n_\alpha u_\alpha\right)=0\,, \tag{5.4}$$

$$\partial_t u_\alpha + \left(e Z_\alpha m_\alpha^{-1}\right)\partial_r\phi + \partial_r\psi + \left(m_\alpha n_\alpha\right)^{-1}\partial_r\left(P_\alpha\right)=0\,, \tag{5.5}$$

$$P_\alpha = n_\alpha k_B T\,. \tag{5.6}$$

The system closing electrostatic Poisson equation taking into account the electrostatic interactions of all the three species is given as

$$r^{-2}\partial_r\left(r^2\partial_r\phi\right)=\left(e\varepsilon_0^{-1}\right)\left(n_e - Z_l n_l - Z_h n_h\right). \tag{5.7}$$

Likewise, the self-gravitational Poisson equation is written as

$$r^{-2}\partial_r\left(r^2\partial_r\psi\right)=\left(4\pi G\right)\left(\Delta\rho_l + \Delta\rho_h\right). \tag{5.8}$$

All the symbols and values used here are quite in a customary form [26-29, 36, 37]. The notations n_e and u_e denote the number density and flow speed of the electronic species. $e=1.6\times10^{-19}$ C denotes the electronic charge. $m_e=9.1\times10^{31}$kg is the electronic mass. $\hbar=h/2\pi\sim10^{-34}$J s is the reduced Planck constant. P_e denotes the effective electronic pressure, which is composed of the pressure due to the temperature degeneracy, interaction with surrounding nucleons, exchange and correlation interaction. $P_{el}=G_e^{'}n_e/\beta'$ stands for the electronic pressure due to the temperature degeneracy. We employ an explicit function describing the temperature degeneracy parameter defined for the transition between T and T_F in generic notations [26-29] as

$$G_e' = Li_{5/2}\left(-\xi\right)/Li_{3/2}\left(-\xi\right). \tag{5.9}$$

Here, $Li_p(-\xi)$ is the polylogarithmic function with index p and $\xi(\mu,T)=e^{\beta'\mu}=e^{\mu/k_BT}$ [26-29]. The general form of $Li_p(-\xi)$ signifying temperature degeneracy effects [26-29] for $p>0$ is

$$Li_p(-\xi)=-(\Gamma(p))^{-1}\int_0^\infty t^{p-1}\left(e^t\xi^{-1}+1\right)^{-1}dt\,, \tag{5.10}$$

where, $\Gamma(p)=\int_0^\infty x^{p-1}e^{-x}\,dx$ is the gamma function.

For the completely degenerate limit ($\xi\to\infty$), we get

$$G_e'=2(5\delta)^{-1} \text{ where, } \delta=T/T_F\,, \tag{5.11}$$

and for the nearly degenerate limit ($\xi>>1$), we get

$$G_e'=2(5\delta)^{-1}\left\{1-(\pi\delta)^2(12)^{-1}\right\}. \tag{5.12}$$

$k_B=1.38\times10^{-23}$ J K^{-1} is the Boltzmann constant signifying energy-temperature correlationship. $P_{ie}=1.8(1/8\pi)(4\pi/3)^{4/3}Z^{2/3}e^2n_e^{4/3}=0.48Z^{2/3}e^2n_e^{4/3}$ gives the resultant pressure due to the interaction of electrons with other neighbouring electrons and surrounding nuclei [8, 9], where Z denotes the atomic number. $P_{exc}=0.916(1/8\pi)(4\pi/3)^{4/3}n_e^{4/3}=0.25e^2n_e^{4/3}$ stands for the pressure due to the electronic exchange interactions [8, 9]. $P_{corr}=(0.0622/6)e^2n_e/a_0=0.0104e^2n_e/a_0$ gives the pressure due to the electronic correlation interactions [8, 9]. $a_0=5.29\times10^{-11}$m is the Bohr unit. It is noted that equation (5.3) is developed specially for modelling white dwarf interiors [8].

As already mentioned above, $\alpha=l$ for the light nuclear species ($^{12}_{6}C$ for CO white dwarf and $^{16}_{8}O$ for ONe white dwarf), and $\alpha=h$ for the heavy nuclear species ($^{16}_{8}O$ for CO white dwarf and $^{20}_{10}Ne$ for ONe white dwarf) in equations (5.4)-(5.6). n_α

and u_α stand for the number density and flow velocity. Z_α denotes their charge states. Likewise, P_α stands for the thermal pressure. ϕ and ψ give the electrostatic and gravitational potentials, respectively. $\varepsilon_0 = 8.85\times10^{-12}$ F m^{-1} denotes the permittivity of the plasma medium. In equation (5.8), $\Delta\rho_l = \rho_l - \rho_{l0} = m_l\left(n_l - n_{l0}\right)$ and $\Delta\rho_h = \rho_h - \rho_{h0} = m_h\left(n_h - n_{h0}\right)$ are used to model the Jeans swindle. $G = 6.67\times10^{-11}$ N m^2 kg^{-2} is the universal gravitational constant.

A number of points regarding the above equations are noteworthy. Equation (5.1) is the equation of continuity depicting the conservation of flux of the electronic species. Equation (5.2) is the force-balancing momentum equation, where the forces due to the electrostatic potential (1st term), electronic pressure (2nd term), and Bohm potential (3rd term) exactly balance each other. It may be highlighted that quantum plasmas are known to occur naturally in dense astrophysical objects, like white dwarfs, Jovian planets, etc., under extreme conditions of temperature and density [42]. When quantum effects start playing a role, the de-Broglie wavelength (λ_B) becomes important. Physically, λ_B represents the spatial extension of the particle wavefunction. Thus, quantum effects start playing a significant role when λ_B becomes similar to or larger than the average interparticle distance ($n^{-1/3}$) [42]. For the ONe white dwarf, the core density is $\sim10^{12}$ kg m^{-3} and core temperature $\sim10^8 - 10^9$ K [6]. Thus, the interparticle distance becomes $\sim10^{-15}$ m. Mathematically, λ_B of the constitutive particles (electrons) is given as $\lambda_B = \hbar/m_e v_T$, where, $v_T = \left(k_B T/m_e\right)^{1/2}$ is the thermal velocity [42]. For ONe white dwarf, one finds by estimation $\lambda_B \sim 10^{-13}$ m. Thus, the de-Broglie wavelength of the constitutive particles is larger than the average interparticle distance, thereby making the inclusion of quantum effects important. This is how quantum-mechanical effects are inevitable in our model consideration. Likewise, for CO white dwarf, the core density is $\sim10^9$ kg m^{-3} and core temperature $\sim10^6 - 10^7$ K [34]. Thus, the interparticle distance becomes $\sim10^{-14}$ m and $\lambda_B \sim 10^{-11}$ m. Thus, even in CO white dwarfs, the incorporation of quantum-mechanical (non-local) effects become equally important as in the previous case.

In constructing a fluid model formalism for quantum plasmas ($n\lambda_B^3 \geq 1$), in contrast to the hydrodynamical equations for classical plasmas ($n\lambda_D^3 \geq 1$), a fundamental difference lies in the addition of the Bohm potential term in the fluid momentum equation modelling the former [43]. While mathematically, the Bohm potential is equivalent to a pressure to be inserted in the momentum transport (force-balancing) equation; physically, it indeed corresponds to typical quantum-mechanical phenomena, such as tunneling, wave packet spreading, propensity to quantum overlapping, etc [43]. Therefore, it is not exactly a pressure in the purely thermodynamical sense [43]. Besides, several quantum plasma models, applicable in similar scenarios of dense plasmas, like white dwarfs, neutron stars, etc., have simultaneously incorporated the effects of the Bohm potential and exchange-correlation terms in the basic governing equations [16, 19, 20]. Thus, the inclusion of the Bohm potential term in our quantum plasma fluid model is quite judicious. Besides, equation (5.3) is the equation of state for the electronic species, taking into account the pressures due to temperature degeneracy (1st term), interaction of electrons with other electrons and surrounding nuclei (2nd term), exchange interaction (3rd term), and correlation interaction (4th term). It is a well-known fact that the white dwarf core is completely degenerate due to extreme conditions of temperature and density [42]. In the planetary nebula, the particles are not as tightly packed as the core, and hence, treated classically. A parameter $\chi = T_F/T$ must be defined in order to express the degeneracy of the system [44]. Since, $\chi = (1/3)\left(3\pi^2 n\lambda_B^3\right)^{2/3}$, the quantum degeneracy becomes important when $\chi \geq 1$ or $n\lambda_B^3 \geq 1$. Thus, in the completely degenerate core, T_F becomes more significant than T. We assume that the shift from classical completely non-degenerate nebula (where T is dominant) to completely degenerate white dwarf core (where T_F is dominant) has a transition region of intermediate degeneracy (surrounding the core) that describes the shift between T and T_F. This explains the physical reason for the first term. The next term takes into account the pressure due to the interaction of electrons with surrounding electrons and other ions. The third and the fourth term take into account the contribution due to the exchange and correlation interaction, respectively. The exchange energy is a direct consequence of the Pauli exclusion principle [8, 9]. As a result, electrons with same spin tend to repel each other. In other words, electrons having same

spins already repel each other, thereby reducing the Coulomb repulsion that would otherwise exist between them in absence of the same spin condition [8, 9]. Correlation interaction gives a metric to determine how much the mobility of one electron is influenced by the presence of the surrounding electrons [9-11]. Equation (5.4) denotes the equation of continuity for the classical species (light nuclear species + heavy nuclear species). Likewise, equation (5.5) is the analog of equation (5.2), but for classical light nuclear species and heavy nuclear species, where the forces by virtue of their motion (1st term), electrostatic potential (2nd term), gravitational potential (3rd term), and thermal pressure (4th term) are exactly balanced by each other. Equation (5.6) is the equation of state taking into account their thermal pressure. Equations (5.7)-(5.8) give the closure of the system in terms of the electrostatic and self-gravitational Poisson equations, respectively.

For a scale-invariant analysis, we employ a standard astronomical normalization scheme [36-38]. The dimensionless set of the basic governing equations are now cast as

$$\partial_\tau N_e + R^{-2}\partial_R\left(R^2 N_e M_e\right)=0, \tag{5.13}$$

$$N_e\partial_R\Phi-\left(p^*_{dp}N_e^{\frac{2}{3}}\partial_R N_e - p^*_{ie}N_e^{\frac{1}{3}}\partial_R N_e - p^*_{exc}N_e^{\frac{1}{3}}\partial_R N_e - p^*_{corr}\partial_R N_e\right)$$
$$-4^{-1}H'^2M_{Fe}^2\left(\partial_R^3 N_e + 2R^{-1}\partial_R^2 N_e - 2R^{-2}\partial_R N_e\right)=0, \text{(for completely degenerate case)} \tag{5.14.1}$$

$$N_e\partial_R\Phi-\left(G_e{}'T^*\partial_R N_e - p^*_{ie}N_e^{\frac{1}{3}}\partial_R N_e - p^*_{exc}N_e^{\frac{1}{3}}\partial_R N_e - p^*_{corr}\partial_R N_e\right)$$
$$-4^{-1}H'^2M_{Fe}^2\left(\partial_R^3 N_e + 2R^{-1}\partial_R^2 N_e - 2R^{-2}\partial_R N_e\right)=0\,. \text{(for nearly degenerate case)} \tag{5.14.2}$$

The dynamics of the classical light nuclear species in normalized form are given as

$$\partial_\tau N_l + R^{-2}\partial_R\left(R^2 N_l M_l\right)=0, \tag{5.15}$$

$$N_l\partial_\tau M_l + N_l\partial_R\Phi + N_l\partial_R\psi + A_{el}\partial_R\left(N_l T^*\right)=0\,. \tag{5.16}$$

Analogously, the dynamics of the heavy nuclear species in normalized form are given as

$$\partial_\tau N_h + R^{-2}\partial_R\left(R^2 N_h M_h\right) = 0\,, \tag{5.17}$$

$$N_h\partial_\tau M_h + N_h\beta\,\partial_R\Phi + N_h\partial_R\psi + A_{eh}\partial_R\left(N_h T^*\right) = 0\,. \tag{5.18}$$

The system closing electrostatic and self-gravitational Poisson equations in dimensionless forms are respectively given as

$$R^{-2}\partial_R\left(R^2\partial_R\Phi\right) = N_e\left(1+\mu'\right) - N_l - \mu' N_h\,, \tag{5.19}$$

$$R^{-2}\partial_R\left(R^2\partial_R\Psi\right) = \sigma\left\{\left(N_l - 1\right) + \mu'\beta^{-1}\left(N_h - 1\right)\right\}. \tag{5.20}$$

In the above equations (5.13)-(5.20), the spatial coordinate is normalized as $R = r/\lambda_{Dl}$; where, $\lambda_{Dl} = \left(m_e c^2\varepsilon_0/\, n_{l0}Z_l e^2\right)^{1/2}$ is the light nuclear Debye length. The temporal coordinate is normalized as $\tau = t/\omega_{pl}^{-1}$; where, $\omega_{pl} = \left(n_{l0}Z_l^2 e^2/m_l\varepsilon_0\right)^{1/2}$ is the light nuclear plasma oscillation frequency. Normalized population density of the constitutive particles is given as $N_s = n_s/n_{s0}$; where, n_{s0} is the equilibrium population density, s being e, l, h for the electronic species, light nuclear species, and heavy nuclear species respectively. Normalized form of flow velocity is given by $M_s = u_s/C_l$; where, $C_l = \left(Z_l m_e c^2/m_l\right)^{1/2}$ is the light nuclear transit speed. The normalized completely degenerate pressure coefficient is given as $p_{dp}^* = p_{dp}/m_e c^2$; where, $p_{dp} = 1.51e^2 n_{e0}^{2/3}$ is the completely degenerate pressure coefficient. The normalized pressure coefficient due to interaction of electrons with other electrons and nuclei is given as $p_{ie}^* = p_{ie}/m_e c^2$; where, $p_{ie} = 0.64\,Z^{2/3}e^2 n_{e0}^{1/3}$ is the unnormalized pressure coefficient due to similar electronic interactions. The normalized pressure coefficient due to electronic exchange interaction is given as $p_{exc}^* = p_{exc}/m_e c^2$; where, $p_{exc} = 0.33e^2 n_{e0}^{1/3}$ is the unnormalized pressure coefficient resulting from exchange interaction. $p_{corr}^* = p_{corr}/m_e c^2$ gives the normalized pressure coefficient due to electronic correlation interaction. Here,

$p_{corr} = 0.0104 e^2/a_0$ is the unnormalized pressure coefficient due to correlation interaction of the electrons. $T^* = Tk_B/m_e c^2$ is the normalized temperature. $H' = \hbar\omega_{pl}/m_e v_{Fe}^2$ is the quantum parameter signifying the ratio of the plasmon energy associated with the light nuclear species to that of the electronic Fermi energy associated. The Fermi Mach number is given as $M_{Fe} = v_{Fe}^2/C_l\, c$; where, v_{Fe} is the Fermi velocity. $\beta = Z_h m_l/Z_l m_h$ is the relative nuclear charge-to-mass coupling parameter. $\mu' = Z_h n_{h0}/Z_l\, n_{l0}$ is the ratio of the charge densities of the heavy-to-light nuclear species. $A_{el} = m_e c^2/m_l C_l^2$ stands for the ratio of the relativistic electronic energy to that of the light nuclear species energy. $A_{eh} = m_e c^2/m_h C_l^2$ is the analogous term for the heavy nuclear species. The ratio of the square of the Jeans frequency to light nuclear plasma oscillation frequency is given as $\sigma = \omega_{Jl}^2/\omega_{pl}^2$; where, $\omega_{Jl} = \left(4\pi G m_l n_{l0}\right)^{1/2}$ is the light nuclear Jeans frequency. The normalized gravitational potential $\Psi = \psi/C_l^2$. $\Phi = \phi e/m_e c^2$ is the normalized electrostatic potential.

5.3 LINEAR STABILITY ANALYSIS

The relevant physical fluid parameters (F) for the plasma fluid are linearly perturbed (F_1) about their hydrostatic homogeneous equilibrium values (F_0) using a normal spherical mode analysis [45] in an auto-normalized Fourier form given as

$$F(R,\tau) = F_0 + F_1(R,\tau) = F_0 + F_{10}\left(R^{-1}\right)\exp\left[-i\left(\Omega\tau - k^* R\right)\right], \tag{5.21}$$

$$F = \left[N_s \quad M_s \quad \Phi \quad \Psi\right]^T, \tag{5.22}$$

$$F_0 = \left[1 \quad 0 \quad 0 \quad 0\right]^T, \tag{5.23}$$

$$F_1 = \left[N_{s1} \quad M_{s1} \quad \Phi_1 \quad \Psi_1\right]^T. \tag{5.24}$$

The spatial and temporal operators get modified in the defined Fourier space $\left(\Omega, k^*\right)$ as $\partial/\partial R \to \left(ik^* - 1/R\right)$ and $\partial/\partial\tau \to \left(-i\ \Omega\right)$. Here, $\Omega\ \left(=\omega/\omega_{pl}\right)$ denotes the normalized fluctuation frequency and $k^*\left(=k/2\pi\lambda_{Dl}^{-1}\right)$ designates the normalized wavenumber. The relevant fluid parameters appearing in equations (5.13)-(5.20) in the new wave-space can be written as

$$N_{e1} = -i\Omega^{-1}\left(ik^* + R^{-1}\right)M_{e1}, \tag{5.25}$$

$$M_{e1} = i\Omega\Phi_1\left\{\left(ik^* + R^{-1}\right)\left(P_e^* - 4^{-1}H'^2M_{Fe}^2\right)\right\}, \tag{5.26}$$

$$N_{l1} = -i\Omega^{-1}\left(ik^* + R^{-1}\right)M_{l1}, \tag{5.27}$$

$$M_{l1} = \left\{\left(ik^* + R^{-1}\right)\Phi_1 - i\sigma\mu'\left(\Omega\beta k^{*^2}\right)^{-1}\left(k^{*^2} + R^{-2}\right)M_{h1}\right\}L^{-1}, \tag{5.28}$$

$$N_{h1} = -i\Omega^{-1}\left(ik^* + R^{-1}\right)M_{h1}, \tag{5.29}$$

$$M_{h1} = -\left(ik^* - R^{-1}\right)\left\{\beta - i\sigma\left(k^{*^2} + R^{-2}\right)\left(\Omega k^{*^2}L\right)^{-1}\right\}\Phi_1H^{-1}, \tag{5.30}$$

$$\Phi_1 = -k^{*^{-2}}\left\{\left(1+\mu'\right)N_{e1} - N_{l1} - \mu'N_{h1}\right\}, \tag{5.31}$$

$$\Psi_1 = -\sigma k^{*^{-2}}\left(N_{l1} + \mu'\beta^{-1}N_{h1}\right). \tag{5.32}$$

In the above set of equations, the various substituted terms in an expanded form are given as

$$P_e^* = p_{dp}^* - p_{ie}^* - p_{exc}^* - p_{corr}^* \quad \text{(for the completely degenerate case)}, \tag{5.33.1}$$

$$P_e^* = G_e{}'T^* - p_{ie}^* - p_{exc}^* - p_{corr}^* \quad \text{(for the nearly degenerate case)}, \tag{5.33.2}$$

$$L = i\left\{\Omega - \Omega^{-1}\left(k^{*^2} + R^{-2}\right)\left(A_{el}T^{*} - \sigma k^{*^{-2}}\right)\right\}, \tag{5.34}$$

$$H = -i\Omega + \left(k^{*^2} + R^{-2}\right)\left[-i\Omega^{-1}\left\{\sigma\mu'\left(\beta k^{*^2}\right)^{-1} - A_{eh}T^{*}\right\} - \sigma^2\left(k^{*^2} + R^{-2}\right)\left(\Omega^2 k^{*^2}\beta L\right)^{-1}\right]. \tag{5.35}$$

A standard procedure of algebraic elimination and simplification among equations (5.25)-(5.32) yields a generalized linear (sextic) dispersion relation on the electrodynamic spatiotemporal response scales of the constitutive light nuclear species with all the generic notations [36, 38] given as

$$\Omega^6 + A_4\Omega^4 + A_2\Omega^2 + A_0 = 0\,. \tag{5.36}$$

The different coefficients appearing in equation (5.36) can be written in an expanded form as

$$A_4 = \left(k^{*^2} + R^{-2}\right)\Big\{-Ek^{*^2}T^{*}\left(2A_{el} + A_{eh}\right) + E\sigma\left(2 + \mu'\beta^{-1}\right) + \left(1 + \mu'\right)\Big\{-2A_{el}T^{*} + \sigma k^{*^{-2}}\left(2 + \mu'\beta^{-1}\right)$$
$$- A_{eh}T^{*} - E\Big\}\Big]\left[Ek^{*^2} + \left(1 + \mu'\right)\right]^{-1}, \tag{5.37}$$

$$A_2 = \left(k^{*^2} + R^{-2}\right)^2\Big[2Ek^{*^2}A_{el}A_{eh}T^{*^2} - 2E\sigma\left\{A_{eh}T^{*} + \left(1 + \mu'\beta^{-1}\right)A_{el}T^{*}\right\} + E\sigma^2 k^{*^{-2}}\left(1 + \mu'\beta^{-1}\right)$$
$$+ Ek^{*^2}\left(A_{el}T^{*}\right)^2 - 2\sigma k^{*^{-2}}\left(1 + \mu'\right)\left\{\left(1 + \mu'\beta^{-1}\right)A_{el}T^{*} + A_{eh}T^{*}\right\} + \left(1 + \mu'\right)A_{el}T^{*^2}\left(2A_{eh} + A_{el}\right)$$
$$+ \left(\sigma k^{*^{-2}}\right)^2\left(1 + \mu'\right)\left(1 + \mu'\beta^{-1}\right) + ET^{*}\left(A_{el} + A_{eh}\right) - \sigma k^{*^{-2}}\left(E + \mu'\beta^{-1}\right) + 2\mu'\beta E\left(A_{el} - \sigma k^{*^{-2}}\right)$$
$$+ 2E\mu'\sigma k^{*^{-2}}\Big]\left[Ek^{*^2} + \left(1 + \mu'\right)\right]^{-1}, \tag{5.38}$$

$$A_0 = \left(k^{*^2} + R^{-2}\right)^3\left[EA_{el}A_{eh}T^{*^2}\left(2\sigma - A_{el}T^{*}k^{*^2}\right) - \sigma^2 k^{*^{-2}}T^{*}\left(A_{eh} + \mu'\beta^{-1}A_{el}\right)\left\{E + \sigma^2 k^{*^{-2}}\left(1 + \mu'\right)\right\}\right.$$
$$+ E\sigma\mu'\beta^{-1}\left(A_{el}T^{*}\right)^2 - \left(1 + \mu'\right)A_{el}^2A_{eh}T^{*^3} - \sigma\mu'\left(1 + \mu'\right)\left(A_{el}T^{*}\right)^3\left(\beta k^{*^2}\right)^{-1} + E\sigma\mu'\left(\beta k^{*^2}\right)^{-1}\left(1 - 2\sigma k^{*^{-2}}\right)$$
$$\left. + EA_{eh}T^{*}\left(\sigma k^{*^{-2}} - A_{el}T^{*}\right) + \mu'\left(\sigma k^{*^{-2}}\right)^2\left(2E - \beta^{-1}\right) + \mu'\beta E\left\{\left(A_{el}T^{*}\right)^2 + \left(\sigma k^{*^{-2}}\right)^2\right\}\right.$$

$$-2E\mu'\sigma k^{*-2}A_{el}T^{*}\left(1+\beta\right)\Big]\Big[Ek^{*2}+\left(1+\mu'\right)\Big]^{-1}. \tag{5.39}$$

In equations (37)-(39), $E=P_e^{*}-4^{-1}H'^{2}M_{Fe}^{2}k^{*}$. (5.40)

For our instability analysis, equation (5.36) with the relevant Ω-moderation of current interest ($\Omega^{q}=0\,\forall q>2$) can be written as

$$A_2\Omega^2+A_0=0\ . \tag{5.41}$$

It is worth mentioning here that the mathematical expressions for $A_2=A_2\left(R,k^{*}\right)$ and $A_0=A_0\left(R,k^{*}\right)$ are already given by equations (5.38) and (5.39), respectively. A number of interesting white dwarf features are clearly evident from the reduced dispersion relation (equation (5.41)). We use $\Omega=\left(1\Omega_r+i\Omega_i\right)$ to characterize the nucleus-acoustic wave instability behaviours. Here, Ω_r (normal) characterizes the propagatory aspects (where, $v_p=\Omega_r/k^{*}$, $v_g=d\Omega_r/dk^{*}$). In contrast, Ω_i (perturbation) depicts the growth/damping behaviour of the same by making the wave amplitude modulated by a factor of $\exp(\pm\Omega_i\tau)$ [46]. It is evident from equations (5.38)-(5.41) that the dynamics of the nucleus-acoustic waves in the completely degenerate states of ONe and CO cores; and their nearly degenerate transition regions is influenced by the concentrations of the constituent species, their mutual electrostatic interactions, temperatures, and so forth.

5.4 RESULTS AND DISCUSSIONS

The stability, propagatory, and dispersive nature of the nucleus-acoustic waves in the completely degenerate ONe and CO white dwarf cores and the nearly degenerate transition regions are analyzed herein using a three-component quantum hydrodynamic plasma model. The quantum electronic species evolves under the conjoint pressures due to temperature degeneracy, interaction with surrounding electrons and other nuclei, exchange energy, and correlation energy. Likewise, the classical thermal pressures are retained for the larger classical species (light nuclear species + heavy nuclear species).

A normal spherical mode analysis yields a generalized linear sextic dispersion relation (equation (5.36)), which is modified using the low-frequency approximation (equation (5.41)). A numerical illustrative platform is provided to reveal the nature of the derived dispersion relation (equation (5.41)). The growth rate corresponding to the nucleus-acoustic wave instability, its propagatory and dispersive features are illustrated pictorially in figures 5.1-5.20. To get a clear idea of the dispersive nature, we use illustrative Matlab profiles depicting the phase dispersion and group dispersion, in addition to the phase and group velocities. The different input values used herein have been calculated using preliminary data available in different trustworthy literary sources [3, 26-29, 32, 34, 47].

5.4.1 Analysis of the completely degenerate ONe core

In figure 5.1, we depict the profile structures of the normalized real angular frequency (Ω_r) (Fig. 1(a)) and normalized imaginary angular frequency (Ω_i) (figure 5.1(b)) with the normalized angular wavenumber (k^*) for different values of the thermodynamic temperature (*T*). The different coloured lines link to Ω_r for $T = 6\times10^9$ K (blue solid line), $T = 7\times10^9$ K (red dashed line), and $T = 8\times10^9$ K (black dotted line). Figure 5.1 clearly shows that Ω_i exists in the low k^*-space (figure 5.1(b)), indicating an unstable behaviour. For a given value of T, Ω_i increases with increasing k^*, becomes maximum, and then decreases to zero. For gradually increasing values of T, the k^*-value at which Ω_i attains peak shifts towards the left side of the k^*-axis, that is, towards smaller k^*-values. As we proceed towards higher values of k^*, we have Ω_r (figure 5.1(a)), indicating the propagatory nature of nucleus-acoustic waves.

Figure 5.2 depicts the profile of the phase velocity (v_p) in the same conditions as figure 5.1. The different coloured lines link to different v_p for $T = 6\times10^9$ K (blue solid line), $T = 7\times10^9$ K (red dashed line), and $T = 8\times10^9$ K (black dotted line). It is clearly seen that for a value of T, v_p increases with k^*. Thus, v_p depends on k^*, indicating the dispersive nature of the system [46, 48-50]. v_p gives the speed of travelling waves. In other words, v_p denoted by the blue solid line indicates the velocity

of the nucleus-acoustic wave at $T = 6\times10^9$ K, and so on. Higher the T of the core, higher is the v_p, and vice-versa.

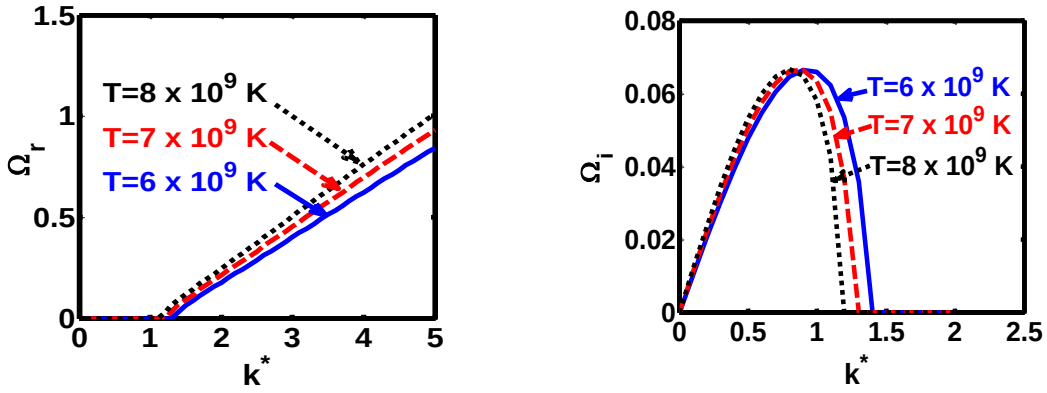

Figure 5.1: *Profile of the normalized (a) real angular frequency(Ω_r) and (b) imaginary angular frequency (Ω_i) with the normalized angular wavenumber (k^*) for different values of the thermodynamic temperature (T) in the completely degenerate case of the ONe white dwarf core.*

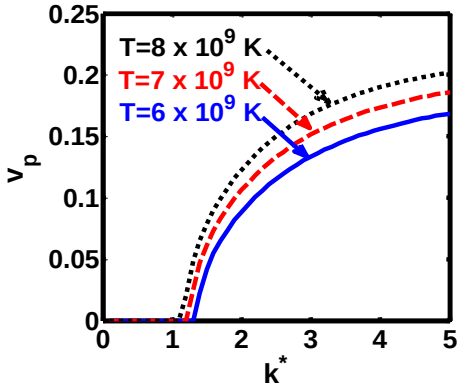

Figure 5.2: *Profile of the normalized nucleus-acoustic wave phase velocity (v_p) in the same conditions as figure 5.1.*

Figure 5.3 depicts the group velocity (v_g) profile with variation in k^* for different indicated values of T. Different coloured lines correspond to different v_g for $T = 6\times10^9$ K (blue solid line), $T = 7\times10^9$ K (red dashed line), and $T = 8\times10^9$ K (black dotted line). Considering the clearly visible trends depicted by figure 5.3(a), it can be fairly commented that for a given value of T, v_g first forms a peak, then

decreases and becomes almost constant with increasing k^*. As the value of T increases, v_g-peak increases and vice-versa (figure 5.3(b)). It is a well-known fact that v_g is the velocity at which a bump travels in a wave [50]. In general, the macroscopic nucleus-acoustic wave propagates through the plasma medium consisting of spectral components of many different acoustic frequencies. If these components are to travel together, then they form a bump as per the wave packet model. A bump is essentially the point at which the phases of the different components become equal and thus, add constructively forming a peak. However, due to different speeds and phases of the different components, the peak gradually dissolves. A second peak may be observed when the phase and amplitude coordinations among the different components take place [48-50].

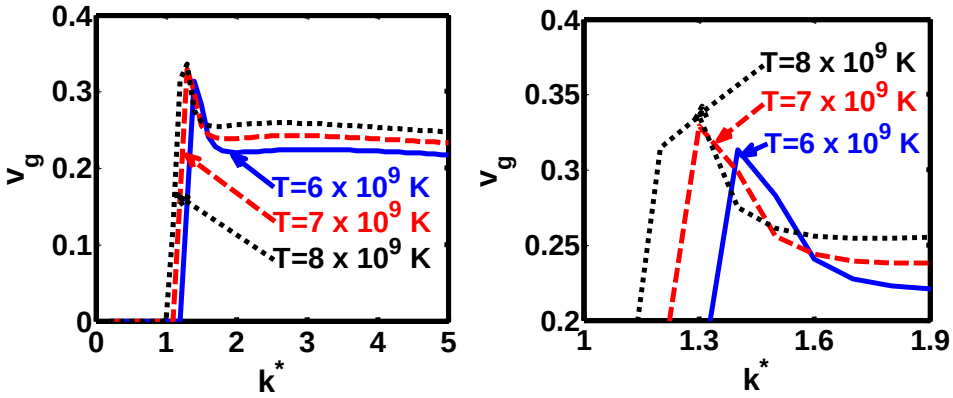

Figure 5.3: *Profile of the normalized nucleus-acoustic wave group velocity* (v_g) *in the same conditions as figure 5.1. The distinct panels depict* v_g *in: (a)* $k^* = 0-5$ *and (b)* $k^* = 1-1.9$.

Figure 5.4 gives the profile of the phase dispersion ($D_p = \partial_{k^*} v_p$) [46, 49] in the same conditions as figure 5.1. As clearly indicated, the different lines connect to different D_p for $T = 6\times10^9$ K (blue solid line), $T = 7\times10^9$ K (red dashed line), and $T = 8\times10^9$ K (black dotted line). Gradually increasing T leads to gradual D_p enhancement. However, the k^*-value at which D_p attains peak (maxima) shifts towards left with increase of T (as clearly indicated by figure 5.4(b)). Figure 5.4(c) depicts the

magnified version in the range $k^* = 4.2 - 5$. The dispersive nature of the system in terms of the nucleus-acoustic wave response is further confirmed in figure 5.4.

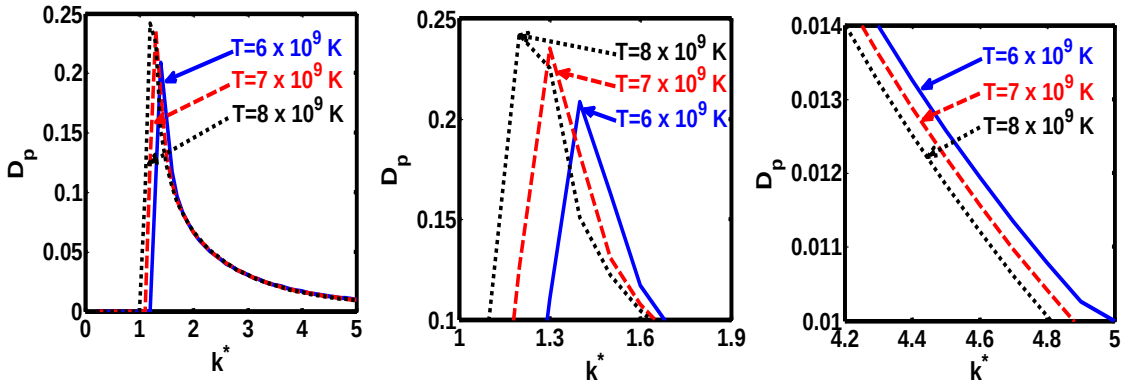

Figure 5.4: *Profile of the nucleus-acoustic wave phase dispersion* (D_p) *in the same conditions as figure 5.1. The distinct panels give* D_p *in: (a)* $k^* = 0 - 5$, *(b)* $k^* = 1 - 1.9$, *and (c)* $k^* = 4.2 - 5$.

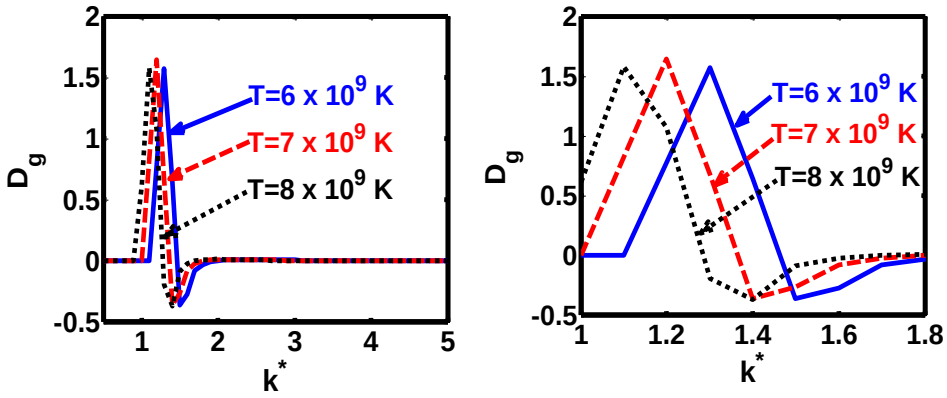

Figure 5.5: *Profile of the nucleus-acoustic wave group dispersion* (D_g) *in the same conditions as figure 5.1. The distinct panels give* D_g *in: (a)* $k^* = 0 - 5$ *and (b)* $k^* = 1 - 1.8$.

In figure 5.5, we depict the group dispersion ($D_g = \partial_{k^*} v_g$) [46, 49] in the same conditions as figure 5.1. The different lines link to different D_g for $T = 6 \times 10^9$ K (blue solid line), $T = 7 \times 10^9$ K (red dashed line), and $T = 8 \times 10^9$ K (black dotted line). As we proceed from $k^* = 1$ towards $k^* = 1.3$, we observe that D_g lines tend to decrease,

that is frequency shift and D_g follow opposite trends, implying an unstable situation [45]. However, on moving towards right starting from $k^* = 1.3$, D_g starts to increase again with increase of k^*, implying a propagatory nature. This further confirms the obtained k^*-range (figure 5.1) for Ω to show unstable (Ω_i) and propagatory (Ω_r) behaviours.

5.4.2 Analysis of the nearly degenerate transition region around ONe core

Figure 5.6 shows the same as figure 5.1, but for the nearly degenerate transition region around the ONe core. The colour coding of the three lines is the same as figures 5.1-5.5. As in figure 5.1, we find that Ω_i exists for lower k^*-values (figure 5.6(b)). In figure 5.6(b), for a particular *T*, Ω_i first increases, becomes maximum and then decreases back. As *T* gradually increases, the peak at which Ω_i becomes maximum shifts towards the left side in the k^*-axis. As we move towards right in the k^*-axis, that is, as the value of k^* increases, we have real values of Ω, that is, Ω_r (figure 5.6(a)), which indicates propagatory behaviour of the nucleus-acoustic wave in the high-k^* space. A spike is observed in both the figures 5.6(a)-5.6(b), unlike previous figures 5.1(a) and 5.1(b).

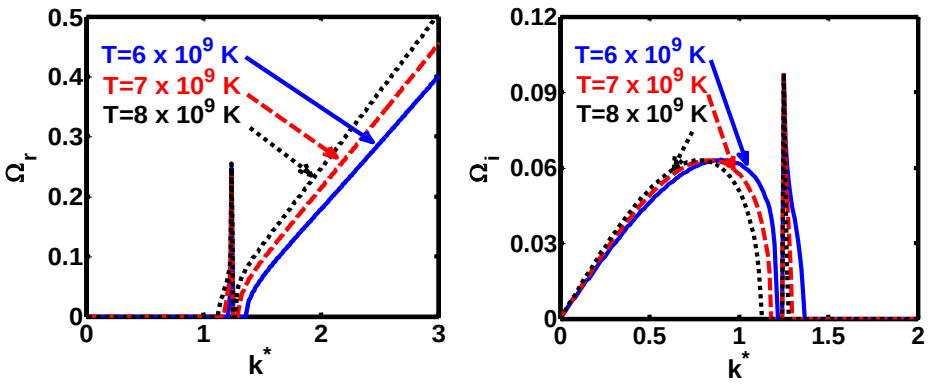

Figure 5.6: *Same as figure 5.1, but for the nearly degenerate case.*

Figure 5.7 shows the same as figure 5.2, but for the borderline region around the core. The different coloured lines indicate that v_p increases with increasing k^*, thereby showing that v_p depends on k^*. Thus, the system is dispersive. It is also observed that

v_p increases with increasing *T*. In other words, higher *T* indicates higher v_p, and vice-versa, same as the completely degenerate core (figure 5.2).

Figure 5.8 shows the same as figure 5.3, but for the surrounding nearly degenerate borderline region depicting the transition between *T* and T_F. It is clearly seen from figure 5.8(a) that v_g forms a peak and then decreases and becomes almost constant with gradually increasing k^*. However, as *T* gradually increases, v_g decreases (figure 5.8(b)), in contrast to the completely degenerate ONe core (figure 5.3). Thus, the point at which the phases of the different components of the wave add up constructively to form a peak is lower for higher *T*. Thus, in the nearly degenerate borderline region, v_g decreases with increasing *T*.

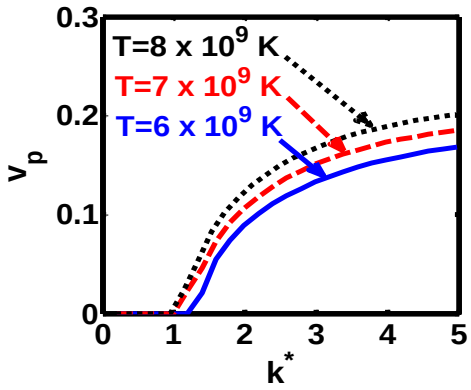

Figure 5.7: *Same as figure 5.2, but for the nearly degenerate case.*

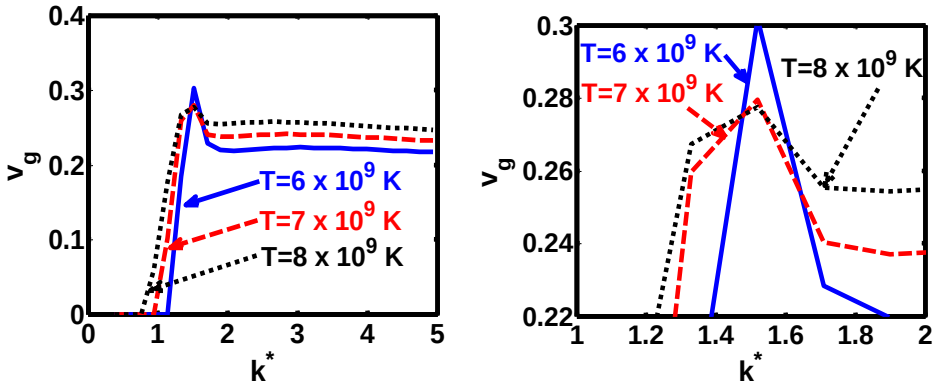

Figure 5.8: *Same as figure 5.3, but for the nearly degenerate case. The distinct panels depict the same in: (a)* $k^* = 0-5$ *and (b)* $k^* = 1-2$.

In a similar fashion, figure 5.9 shows the same as figure 5.4, but for the nearly degenerate region around the core. The D_p profiles further confirm the dispersive nature of the plasma. It is seen that the features exhibited by the D_p curves in the nearly degenerate surrounding of the core are the same as that in completely degenerate core (figure 5.4). D_p increases with increasing T and the D_p maxima (peak) shifts towards the left of the k^*-axis with T enhancement. Figures 5.9(b) and 5.9(c) show the sectional magnified versions of figures 5.9(a) in the range $k^* = 0.9 - 2$ and $k^* = 4 - 4.8$, respectively.

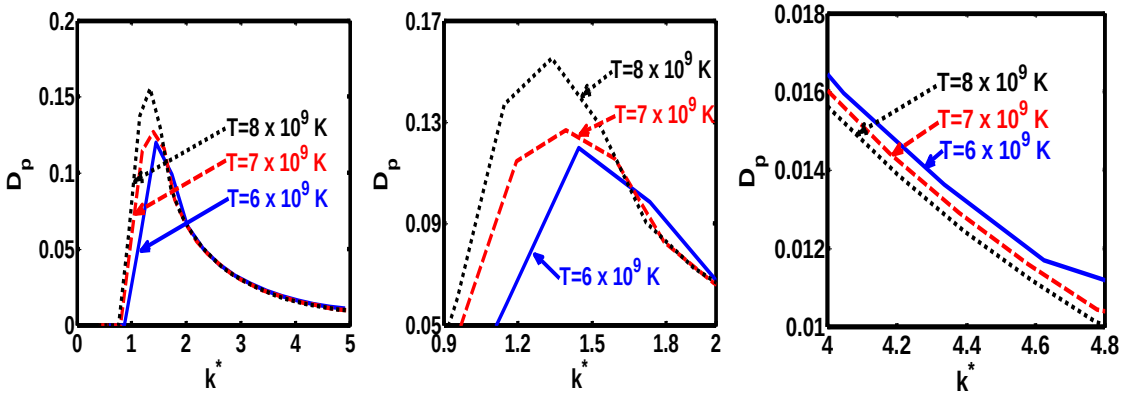

Figure 5.9: *Same as figure 5.4, but for the nearly degenerate case. The distinct panels depict the same in: (a)* $k^* = 0 - 5$ *(b)* $k^* = 0.9 - 2$*, and (c)* $k^* = 4 - 4.8$.

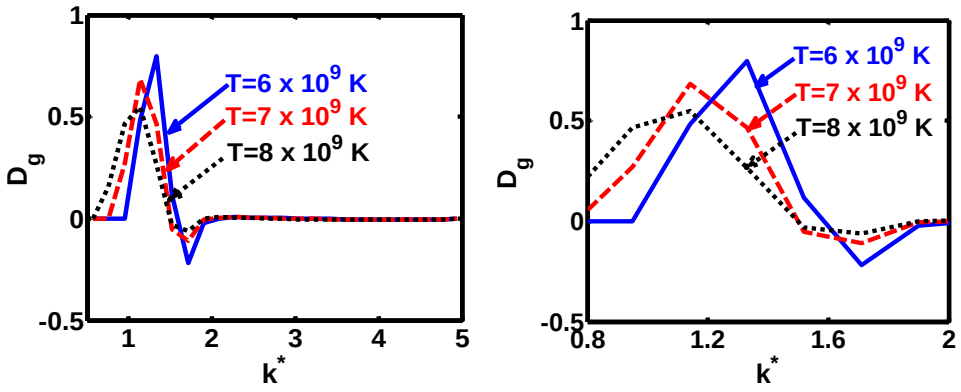

Figure 5.10: *Same as figure 5.5, but for the nearly degenerate case. The distinct panels depict the same in: (a)* $k^* = 0 - 5$ *(b)* $k^* = 1 - 2$.

Likewise, figure 5.10 shows the D_g profile with variation in k^* for different T values, that is, same as figure 5.5, but in the nearly degenerate region. If we proceed from $k^* = 1.2$ towards $k^* = 1.5$, we see that D_g decreases. Thus, D_g and k^* follow opposite trends (D_g decreases with increase of k^*), thereby indicating unstable behaviour in the low-k^* space [49]. However, as we proceed from $k^* = 1.5$ towards right in the k^*-axis, D_g increases. Thus, D_g and k^* follow the same trend, showing a propagatory behaviour in the high-k^* space. This reinforces the accuracy of the trends obtained in figures 5.6(a) and 5.6(b). In other words, Ω_r (propagatory nucleus-acoustic wave) exists from $k^* = 1.5$ onwards (figure 5.6(a)), whereas Ω_i (growing nucleus-acoustic wave) exists in the low-k^* space till $k^* = 1.5$ (figure 5.6(b)).

5.4.3 Analysis of the completely degenerate CO core

Figure 5.11 shows the same as figure 5.1, but for the completely degenerate CO white dwarf cores. The different coloured lines link to different Ω_r (figure 5.11(a)) and Ω_i (figure 5.11(b)) values with variation in k^* for $T = 2\times10^6$ K (blue solid line), $T = 2\times10^7$ K (red dashed line), and $T = 2\times10^8$ K (black dotted line). The observations are the same as the completely degenerate ONe core (figures 5.1(a) and 5.1(b)), that is, for a given T, Ω_i (unstable) exists for the low-k^* values (figures 5.11(b)). Towards high-k^* values, we get Ω_r, which implies propagatory behaviour (figure 5.11(a)). The only difference between figure 5.1 and figure 5.11 is the k^*-range in which Ω shows unstable and propagatory behaviours. The k^*-range in figure 5.11 is much higher than that in figure 5.1.

Figure 5.12 shows the same as figure 5.2, but for the completely degenerate core. The various coloured lines correspond to different v_p for $T = 2\times10^6$ K (blue solid line), $T = 2\times10^7$ K (red dashed line), and $T = 2\times10^8$ K (black dotted line). For a given T, v_p starts increasing from the k^*-point from which Ω_r comes into existence, after which the v_p-curve attains an almost constant value with increasing k^*. That is, v_p

gives the velocity of the propagatory nucleus-acoustic wave. For increasing T, v_p increases and vice-versa. It implies that v_p is k^*-dependent and hence, the system is dispersive [49, 50].

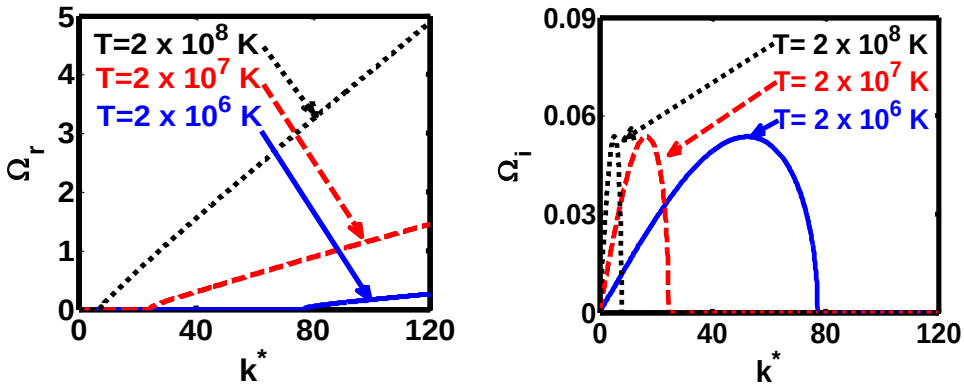

Figure 5.11: *Same as figure 5.1, but for completely degenerate CO white dwarf core.*

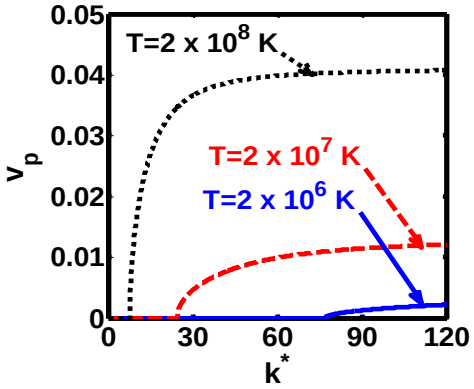

Figure 5.12: *Same as figure 5.2, but for completely degenerate CO white dwarf core.*

Figure 5.13 shows the same as figure 5.3, but for the CO core. The different lines link to different v_g for $T = 2\times10^6$ K (blue solid line), $T = 2\times10^7$ K (red dashed line), and $T = 2\times10^8$ K (black dotted line). For a given T, v_g starts increasing from the k^*-point from which Ω_r comes into existence, attains peak for a very small k^*-range, after which it starts to decrease again. v_g-curve attains an almost constant value with increasing k^* after decreasing from the peak. The peak attained is highest for $T = 2\times10^8$ K, followed by $T = 2\times10^7$ K and so on. With increase of T, the peaks

attained by the v_g-curves shift towards the smaller k^*-values. It clearly shows that the phases of the different components of the nucleus-acoustic wave add up constructively for a very short frequency range, thus forming the v_g-peaks for very small k^*-range.

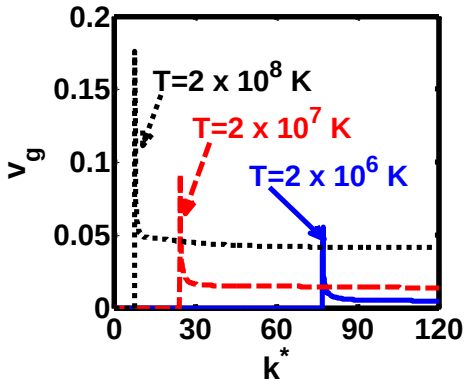

Figure 5.13: *Same as figure 5.3, but for completely degenerate CO white dwarf core.*

The dispersive nature of the considered plasma system is further confirmed by figure 5.14, which shows the same as figure 5.4, but for the completely degenerate CO white dwarf core. As clearly indicated by figures 5.14(a) and 5.14(b), the different coloured lines link to different D_p for $T = 2\times10^6$ K (blue solid line), $T = 2\times10^7$ K (red dashed line), and $T = 2\times10^8$ K (black dotted line). The observations are the same as figure 5.4, except for the fact that the D_p exists for a much higher k^*-range in figure 5.14 than that in figure 5.4. D_p first increases from the k^*-value from which Ω_r comes into existence. It then attains peak and starts to decrease towards very low D_p value. With increase of *T*, the D_p-peak shifts towards low-k^* values and vice-versa (as clearly seen from figure 5.14(a)).

Figure 5.15 shows the same as figure 5.5, but for the completely degenerate CO core. The different lines link to different D_g for $T = 2\times10^6$ K (blue solid line), $T = 2\times10^7$ K (red dashed line), and $T = 2\times10^8$ K (black dotted line). In the low-k^* space, D_g forms a peak and then decreases with increasing k^*. Thus, D_g and k^* follow opposite trends, indicating an unstable situation. However, starting from the point at

which different Ω_r for different T come into existence, the D_g -curves start to increase again with k^*, thus showing propagatory nature of the considered nucleus-acoustic wave. This further re-confirms the obtained k^*-range for existence of Ω_r and Ω_i (figures 5.11(a) and 11(b)).

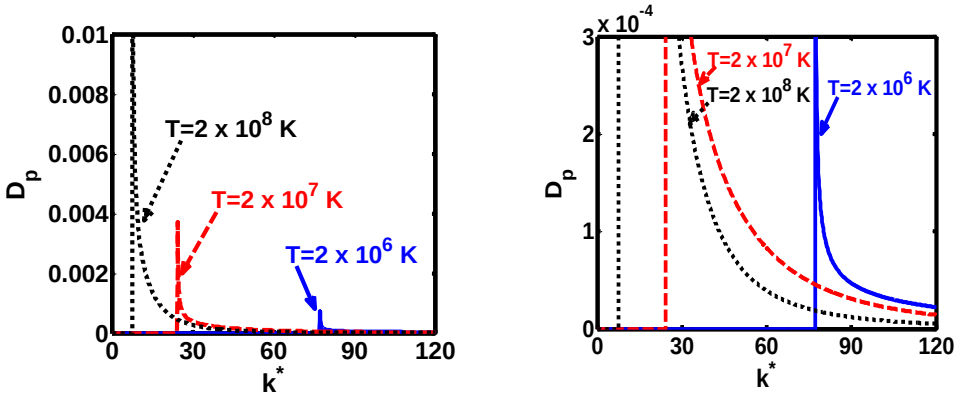

Figure 5.14: *Same as figure 5.4, but for completely degenerate CO white dwarf core.*

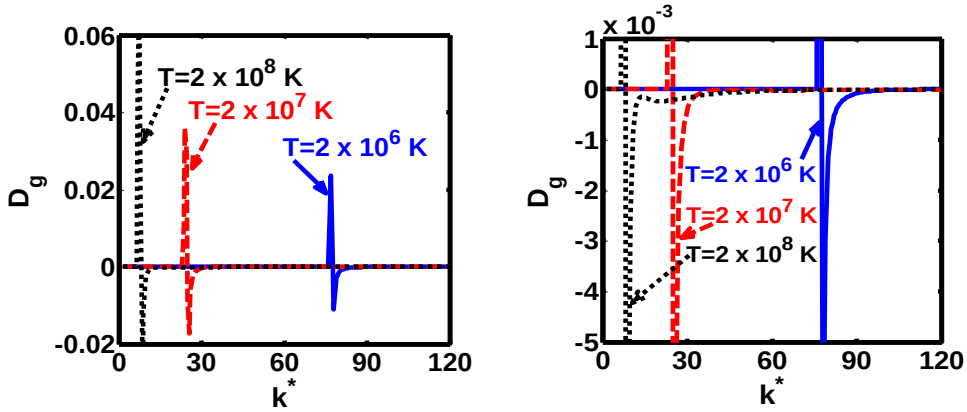

Figure 5.15: *Same as figure 5.5, but for completely degenerate CO white dwarf core.*

5.4.4 Analysis of the nearly degenerate transition region around CO core

Figure 5.16 shows the same as figure 5.6, but for the nearly degenerate transition region around the CO core. The colour coding adopted here is the same as figures 5.11-5.15. It is observed that for the low-k^* space, Ω_i exists for different T (figure 5.16(b)), thereby indicating an unstable behaviour. The Ω_i-peaks shift towards the smaller k^*-values

with increasing T. As we move towards higher k^*-values, Ω_r comes into existence (figure 5.16(a)), indicating the propagatory nature of nucleus-acoustic wave.

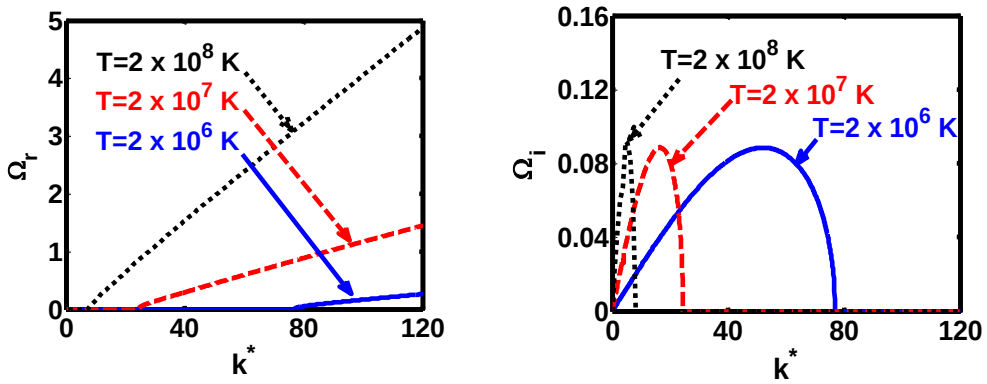

Figure 5.16: *Same as figure 5.6, but for CO nearly degenerate transition region.*

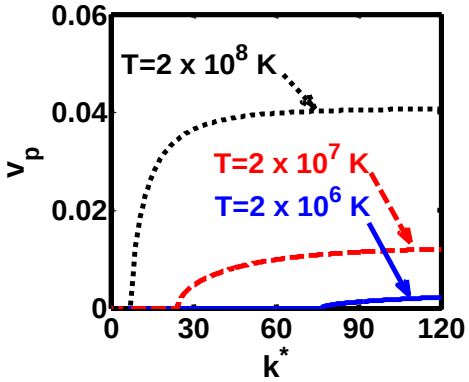

Figure 5.17: *Same as figure 5.7, but for CO nearly degenerate transition region.*

Figure 5.17 shows the same as figure 5.7, but for the nearly degenerate region around the core. It can be clearly observed that v_p depends on k^* for a given T. This clearly hints towards the dispersive nature of the considered plasma system. In addition, v_p increases with increasing T.

Figure 5.18 shows the same as figure 5.8, but for the nearly degenerate transition region around the CO core. The peak at which the phases of the different components of the propagatory nucleus-acoustic wave become equal and add up constructively exists for a very small k^*-range for a particular T. With gradually increasing T, the v_g-peak shifts towards the low k^*-values.

Figure 5.19 depicts the same as figure 5.9, but for the nearly degenerate region around the CO core. The observations are the same as figure 5.9, except for the fact that D_p exists for a much higher k^*-range as compared to figure 5.9. It confirms the dispersive nature of the plasma medium, which is the same as figure 5.9. The D_p-peaks shift towards the lower k^*-values with T enhancement.

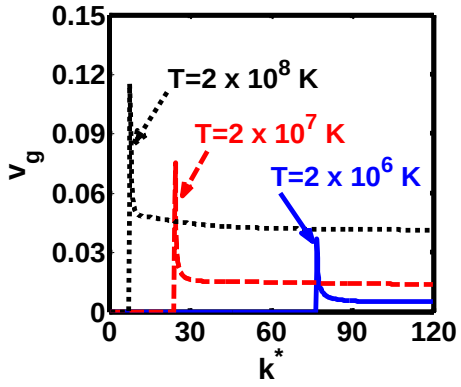

Figure 5.18: *Same as figure 5.8, but for CO nearly degenerate transition region.*

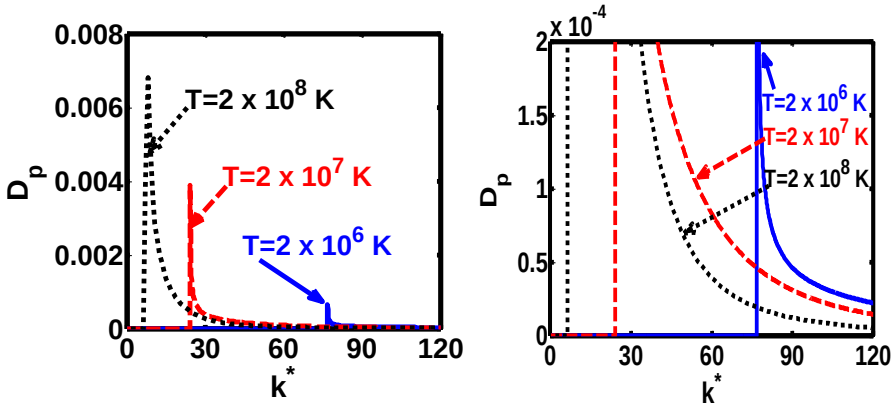

Figure 5.19: *Same as figure 5.9, but for CO nearly degenerate transition region.*

Figure 5.20 shows the same as figure 5.10, but for the borderline region around the completely degenerate CO core. In the low-k^* space, D_g forms a peak and then tends to decrease with increasing k^*. Thus, D_g and k^* follow opposite trends, indicating an unstable situation. However, starting from the point at which different Ω_r for different T come I nto existence, the D_g-curves start to increase again with increase

of k^*, thus showing propagatory nature of the considered nucleus-acoustic wave. This further affirms the obtained k^*-range for the existence of Ω_r and Ω_i (figures 5.16(a) and 5.16(b)).

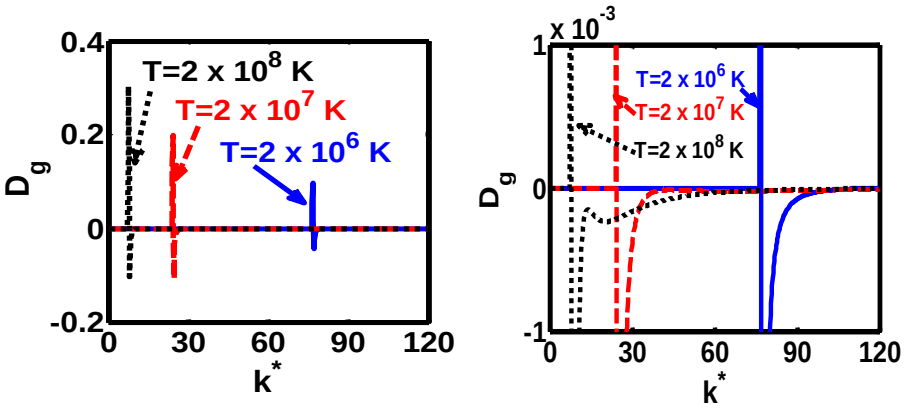

Figure 5.20: *Same as figure 5.10, but for CO nearly degenerate transition region.*

In the obtained scale-free figures 5.1-5.20, k^* signifies a broader space of the auto-normalized wavenumber, $k^* = k/k_{Dl} = k/\left(2\pi\lambda_{Dl}^{-1}\right)$, as per the adopted Fourier transformation (equation (5.21)). Accordingly, the hydrodynamic regime (low-frequency fluctuations) is characterized by a subcritical angular wavenumber defined as $k^* = k/k_{Dl} < 1$. In this purview, the kinetic regime (high-frequency fluctuations) is characterized by a supercritical wavenumber, specified as: $k^* = k/k_{Dl} > 1$. The hybrid (hydrokinetic) class of intermediate collective fluctuations is described by a transcritical wavenumber, $k^* = k/k_{Dl} \approx 1$. As a result, the graphical analysis of the proposed wave instability investigation founded on a generalized hydrodynamic formalism evidently encloses both the extreme regimes of the hybrid nucleus-acoustic wave fluctuations defined clearly by the critical k^*-scalings (as shown parametrically in figures 5.1-5.20). Therefore, we can infer from our analysis that, a microphysically low-frequency (hydrodynamic) regime (decided on the Ω-scale) can macrophysically have mixed-frequency (hydrokinetic) fluctuation counterpart regimes, found on the extreme k^*-scale as critical instability behaviours.

5.5 CONCLUSIONS

A three-component spherically symmetric quantum plasma model is developed to analyze the stability, propagatory, and dispersive behaviour of nucleus-acoustic waves. These modes are excited in the completely degenerate ONe and CO white dwarf cores and their nearly degenerate surrounding envelopes. The model comprises of quantum electrons and classical light-heavy nuclear species assumed initially to lie in a hydrostatic homogeneous equilibrium configuration. The constitutive electrons are acted upon by the pressures due to temperature degeneracy, interaction with surrounding electrons and other nuclei, exchange energy, and correlation energy explicitly. The pressures due to exchange and correlation are purely quantum-mechanical in origin, having no classical analogs. The classical thermal pressure acting upon the light nuclear species and heavy nuclear species are retained in their respective equations of state. A standard normal spherical mode analysis yields a sextic generalized linear dispersion relation for low-frequency fluctuation analysis.

It is seen numerically that for both the completely degenerate core and the nearly degenerate transition region, we find propagatory feature of nucleus-acoustic wave (Ω_r) towards high-k^* space (figures 5.1(a), 5.6(a), 5.11(a), 5.16(a)). Unstable behaviour (Ω_i) exists for the low-k^* space (figures 5.1(b), 5.6(b), 5.11(b), 5.16(b)). The v_p-evolution shows similar trends in both the completely degenerate core and the nearly degenerate envelope for both the dwarfs (figures 5.2, 5.7, 5.12, 5.17). In both the cases, v_p is dependent on k^*, thereby indicating its dispersive nature. In the case of the completely degenerate ONe core, the point at which different components of the propagatory nucleus-acoustic waves add up constructively to form a peak gradually increases with T (figure 5.3), in contrast to nearly degenerate envelope (figure 5.8). However, both the completely degenerate CO core and nearly degenerate transition envelope show a common trend, that is, higher v_g-peaks with increase of T (figures 5.13, 5.18). D_p observed for the completely degenerate core and nearly degenerate ambience of both the ONe and CO white dwarfs re-confirm the dispersive nature of the medium (figures 5.4, 5.9, 5.14, 5.19). The trends observed for D_g for both the ONe and CO completely degenerate cores and nearly degenerate ambience reaffirm the observed

k^*-ranges for the propagatory and unstable behaviour of the proposed nucleus-acoustic wave modes (figures 5.5, 5.10, 5.15, 5.20).

The constitutive electrons in compact astrophysical objects can have their Fermi energy greater than or equal to their rest mass energy (i.e., $k_B T_F \geq m_{e0} c^2$) [52]. It hereby implicates a fundamental requirement for a refined modelling of the presented analysis with the proper incorporation of collective relativistic mechanics [52]. We expect to see significant effects due to all the pressure terms on the plasma system stability upon proper refinement of the proposed model with the inclusion of the said relativistic effects [52, 53].

It may be noteworthy that, unlike the presented pulsational study (radial), several pulsations (angular) have previously been reported in PG1159 pre-white dwarfs, variable DB, and variable DA [2]. In fact, recent investigations reveal that pulsations have been discovered in carbon atmosphere white dwarfs [54]. A large number of parameters of white dwarfs like stellar mass, rotation rates, etc. have been calculated, but so far no attempt has been made to asteroseismologically probe the microphysical dynamics of white dwarfs. It implicates that there are fair possibilities for the detection of the proposed modes in dwarf family stars and closely related compact astrophysical circumstances in the near future with the needful refinements in modern astronomy and space exploration systems [55]. Thus, there is an impending need of state-of-art technology to actually explore the dynamics of the interparticle interactions in white dwarfs [56]. Finally, our theoretic analysis can open an emerging research area on diversified collective waves, oscillations, and instabilities excitable in the ONe and CO white dwarfs and similar compact astrophysical circumstances in an asteroseismic probing perspective rooted in quantum plasma processes [50, 55, 57].

REFERENCES

[1] Shukla, P. K. and Eliasson, B. Nonlinear aspects of quantum plasma physics. *Physics-Uspekhi*. 53(1):51-76, 2010.

[2] Koester, D. White Dwarfs: Recent Developments. *The Astronomy and Astrophysics Review*, 11:33-66, 2002.

[3] Lang, K. R. *Essential Astrophysics*. Springer, Heidelberg, 1st edition, 2013.

[4] Dominguez, I., Straniero, O., Tornambe, A., and Isern, J. On the formation of massive C-O white dwarfs: The lifting effect of rotation. *The Astrophysical Journal*, 472(1):783-788, 1996.

[5] Dutta, A., Sahu, D. K., Anupama G. C., Joharle, S., Kumar, B., Nayana, A. J., Singh, A., Kumar, H., Bhalerao, V., and Barway, S. SN 2020sck: Deflagration in a Carbon-Oxygen White Dwarf. *The Astrophysical Journal*, 925(2):217, 2022.

[6] Isern, J., Canal, R., and Labay, J. The outcome of explosive ignition of ONeMg cores: Supernovae, neutron stars, or "Iron" white dwarfs? *The Astrophysical Journal*, 372:L83-L86, 1991.

[7] Gutiérrez, J., Canal, R., and García-Berro, E. The gravitational collapse of ONe electron-degenerate cores and white dwarfs: The role of ^{24}Mg and ^{12}C revisited. *Astronomy and Astrophysics*, 435(1):231-237, 2005

[8] Auluck, F. C. and Mathur, V. S. Electrostatic interactions in white dwarfs. *Zeitschrift für Astrophysik*, 48:28-33, 1959.

[9] Salpeter, E. E. Energy and pressure of a zero-temperature plasma. *The Astrophysical Journal*, 134(3): 669-682, 1961.

[10] Gell-Mann, M. and Brueckner, K. A. Correlation energy of an electron gas at high density *Physical Review*, 106(2):364-368, 1957.

[11] Takada, Y. *Strongly Coupled Plasma Physics*. Elsevier, North Holland, 1990.

[12] Ma, Y., Mao, S., and Xue, J. Waves in a bounded quantum plasma with electron exchange-correlation effects. *Physics of Plasmas*, 18(10):102108, 2011.

[13] Shahmansouri, M. The exchange-correlation effects on surface plasmon oscillations in semi-bounded quantum plasma. *Physics of Plasmas*, 22(9):092106, 2015.

[14] Khan, A. A., Jamil, M., and Hussain, A. Wake potential with exchange-correlation effects in semiconductor quantum plasmas. *Physics of Plasmas*, 22(9):092103, 2015.

[15] Shahmansouri, M. and Misra, A. P. Elliptically polarized electromagnetic waves in a magnetized quantum electron-positron plasma with effects of exchange-correlation. *Physics of Plasmas*, 23(7):072105, 2016.

[16] Rimza, T. and Sharma, P. Effect of exchange correlation potential on dispersion properties of lower hybrid wave in degenerate plasma. *Journal of Physics: Conference Series*, 836(1):012028, 2017.

[17] Khan, A. A., Zeba, I., Jamil, M. and Asif, M. Oscillatory wake potential with exchange-correlation in plasmas. *Physics of Plasmas*, 24(12):123708, 2017.

[18] Rasheed, A., Jamil, M., Jung, Y. D., Sahar, A., and Asif, M. The exchange-correlation field effect over the magnetoacoustic-gravitational instability in plasmas. *Zeitschrift für Naturforschung A*, 72(10): 915-921, 2017.

[19] Haque, Q. and Shan, S. A. Impact of electron exchange-correlation on drift acoustic solitary waves. *Physics Letters A*, 382(38): 2744-2748, 2018.

[20] Sharma, P. Modified dispersion properties of lower hybrid wave with exchange correlation potential in ultra-relativistic degenerate plasma. *Physics Letters A*, 382(27):1796-1800, 2018.

[21] Chen, S., Li, C., Zha, X., Zhang, X., and Xia, Z. High-frequency surface waves in quantum plasmas with electrons relativistic degenerate and exchange-correlation effects. *Chinese Journal of Physics*, 68:79-86, 2020.

[22] Taghadosi, M. R., Niknam, A. R., and Khorashadizadeh, S. M. Electron-exchange and correlation effects on filamentation instability of a high-density current-driven plasma. *Physics of Plasmas*, 27 (3):032113, 2020.

[23] Haque, Q. Drift and ion acoustic waves in an inhomogeneous electron-positron-ion plasma with temperature degeneracy and exchange-correlation effects. *Results in Physics*, 18:103287, 2020.

[24] Li, C., Zhan, Y., Zhou, B., Zhang, J., and Chen, S. Electron exchange-correlation effects on dispersion properties of electrostatic waves in degenerate quantum plasmas. *Chinese Journal of Physics*, 72:375-385, 2021.

[25] Sadiq, N. and Ahmad, M. Quantum inertial Alfvén solitary waves: the effect of exchange-correlation and spin magnetization. *Waves in Random and Complex Media*, 31(6):2058-2073, 2021.

[26] Jan, Q., Mushtaq, A., Farooq, M., and Shah, H. A. Alfvén solitary waves with effect of arbitrary temperature degeneracy in spin quantum plasma. *Physics of Plasmas*, 25(8): 082122, 2018.

[27] Haas, F. and Mahmood, S. Linear and nonlinear ion-acoustic waves in nonrelativistic quantum plasmas with arbitrary degeneracy. *Physical Review E*. 92(5): 053112, 2015.

[28] Ali, S., Ahmad, M., and Ikram, M. Magnetoacoustic waves with effect of arbitrary degree of temperature and spin degeneracy in electron-positron-ion plasmas. *Contributions to Plasma Physics*, 60(2):1-11, 2019.

[29] Safdar, A., Mushtaq, A., Ikram, M., Ahmad, Z., Batool, S. R. Effect of arbitrary temperature degeneracy and ion magnetization on shear Alfven waves in electron-positron-ion plasmas. *Contributions to Plasma Physics*, 61(2):1-14, 2020.

[30] Truran, J. W. and Livio, M. On the frequency of occurrence of oxygen-neon-magnesium white dwarfs in classical nova systems. *The Astrophysical Journal*, 308:721-727, 1986.

[31] Williams, R. E., Ney, E. P., Sparks, W. M., Starrfield, S. G., Wyckoff, S., and Truran, J. W. Ultraviolet spectral evolution and heavy element abundances in Nova Coronae Austrinae 1981. *Monthly Notices of the Royal Astronomical Society*, 212:753-766, 1985.

[32] Shara, M. M. Masses of white dwarfs in O-Ne-Mg novae: observational constraints, galactic ^{26}Al, ^{22}Na γ-rays, and M31 novae. *The Astronomical Journal*, 107(4):1546-1550, 1994.

[33] Vanlandingham, K. N., Starrfield, S., and Shore, S. N. Elemental abundances for V693 Coronae Austrinae 1981. *Monthly Notices of the Royal Astronomical Society*, 290(1):87-98, 1997.

[34] Fontaine, G., Brassard, P., and Bergeron, P. The potential of white dwarf cosmochronology. *The Publications of the Astronomical Society of the Pacific*, 113(782): 409-435, 2001.

[35] Oskinova, L. M., Gvaramadze, V. V., Gräfener, G. , Langer, N., and Todt, H. X-rays observations of a super-Chandrasekhar object reveal an ONe and a CO white dwarf merger product embedded in a putative SNIax remnant. *Astronomy and Astrophysics*, 644:L8, 2020.

[36] Dasgupta, S. and Karmakar, P. K. Propagatory dynamics of nucleus-acoustic waves excited in gyrogravitating degenerate quantum plasmas electrostatically confined in curved geometry. *Scientific Reports*, 11:19126, 2021.

[37] Karmakar, P. K. and Das, P. Nucleus-acoustic waves: Excitation, propagation, and stability. *Physics of Plasmas*, 25(8): 082902, 2018.

[38] Zaman, D. M. S., Amina, M., Dip, P. R., and Mamun, A. A. Planar and non-planar nucleus-acoustic shock structures in self-gravitating degenerate quantum plasma systems. *European Physical Journal Plus*, 132:457, 2017.

[39] Sultana, S. Review of heavy-nucleus-acoustic nonlinear structures in cold degenerate plasmas. *Reviews of Modern Plasma Physics*, 6:6, 2022.

[40] Koester, D. and Chanmugam, G. Physics of white dwarf stars. *Reports on Progress in Physics*, 53 (7):837-915, 1990.

[41] Koester, D. *Planets, Stars and Stellar Systems*. Springer, Dordrecht, 2013.

[42] Manfredi, G. How to model quantum plasmas. *Field Institute Communications*, 46:263-287, 2005.

[43] Hass, F. *Quantum Plasmas: A Hydrodynamic Approach*. Springer, New York, 2011.

[44] Misra, A. P. and Brodin, G. Wave-particle interactions in quantum plasmas. *Reviews of Modern Plasma Physics*, 6:5, 2022.

[45] Kalita, D. and Karmakar, P. K. Jeans instability in nonideal MHD plasma clouds with geometric curvature effects. *IEEE Transactions on Plasma Science*, 49(7):2042-2047, 2021.

[46] Karmakar, P. K. and Goutam, H. P. The Hall-induced stability of gravitating fluids. *New Astronomy*, 61:84-94, 2018.

[47] Leung, S., Nomoto, K., and Suzuki, T. Electron-capture supernovae of super-AGB stars: sensitivity on input physics. *The Astrophysical Journal*, 889 (1): 34(1)-34(25), 2020.

[48] Bittencourt, J. A. *Fundamentals of Plasma Physics*. Springer, New York, 3rd edition, 2004.

[49] Chen, F. F. *Introduction to plasma physics and controlled fusion*. Plenum Press, New York, 2nd edition, 1984.

[50] Morin, D. *Dispersion*. Retrieved on 18 Nov. 2022 from https://scholar.harvard.edu/files/david-morin/files/waves_dispersion.pdf

[51] March, N. H. The Thomas-Fermi Approximation in Quantum Mechanics. *Advances in Physics*, 6 (21): 1-101, 1957.

[52] Brodin, G. and Zamanian, J. Quantum kinetic theory of plasmas. *Reviews of Modern Plasma Physics*, 6:4, 2022.

[53] Dasgupta, S. and Karmakar, P. K. Relativistic ion-acoustic waves in electrospherically confined gyromagnetoactive quantum plasmas. *Chinese Journal Physics*, 76:299-309, 2022.

[54] Fontaine, G., Brassard, P., Dufour, P., Green, E. M., and Liebert, J. Pulsations in carbon-atmosphere white dwarfs: A new chapter in white dwarf asteroseismology. *Journal of Physics: Conference Series*, 172: 012066, 2009.

[55] Silvotti, R., Fontaine, G., Pavlov, M., Marsh, T. R., Dhillon, V. S., Littlefair, S. P., and Getman, F. Search for p-mode oscillations in DA white dwarfs with VLT-ULTRACAM. I. Upper limits to the p-modes. *Astronomy and Astrophysics*,525: A64, 2011.

[56] Saumon, D., Blouin, S., and Tremblay, P. E. Current challenges in the physics of white dwarf stars. *Physics Reports*, 988:1-63, 2022.

[57] Atteya, A., El-Borie, M. A., Roston, G. D., and El-Helbawy, A. S. Nonlinear dust acoustic waves in an inhomogeneous magnetized quantum dusty plasma. *Waves in Random and Complex Media*, 33(2):329-344, 2021.